ECCOMAS Congress 2016
VII European Congress on Computational Methods in Applied Sciences and Engineering
M. Papadrakakis, V. Papadopoulos, G. Stefanou, V. Plevris (eds.)
Crete Island, Greece, 5–10 June 2016

MULTIPLE TIMESCALE MODELLING OF PARTICLE SUSPENSIONS IN METAL MELTS SUBJECTED TO EXTERNAL FORCES

Anton Manoylov[1], Georgi Djambazov[1], Valdis Bojarevics[1] and Koulis Pericleous[1]

[1] Computational Science and Engineering Group, University of Greenwich
e-mail: A.Manoylov@gre.ac.uk, K.Pericleous@gre.ac.uk,
web: http://cnmpa.gre.ac.uk/group_cseg.html

Keywords: CFD-DEM, particle adhesion, collision predictions, electro-magnetic stirring.

Abstract. *Electro-magnetic (EM) fields are widely used in metallurgy in order to stir conducting metals without the risk of contamination or causing an instability or chemical reaction. During the manufacturing of metal matrix composites (MMC), ceramic micro- and nano-particles are added into the metal melt, and ultrasonic (US) processing and EM stirring are used to break the agglomerates and to enhance the dispersion of the particles. EM stirring can also be used to remove the unwanted particles from liquid metal by pushing them towards the walls of the crucible where they adhere and can be easily removed.*

A model has been developed to account for the complex interaction of the particles with each other, with the walls, as well as with the flow of the metal melt. Particles are modelled as elastic spheres with adhesion. Adhesion is incorporated in the model using the Johnson, Kendal, Robert (JKR) and Derjaguin, Muller, Toporov (DMT) theories. The case of the oblique impact of the particles is modelled according to the Thornton and Yin method based on the partial-slip theory developed by Mindlin & Deresievics. The developed particle model is then coupled with the magneto-hydrodynamics (MHD) code PHYSICA in order to demonstrate the effect of the EM stirring and vibration.

Multiple time-scales are used which permits modelling the realistic time range of metal-processing and at the same time capture the individual collisions between particles with sufficient precision. Several methods of predicting the particle collisions are employed and their efficiency is compared for the case of removing contaminating particles from liquid metal.

1 INTRODUCTION

This research is focused on developing the computational model of interacting particles and particle clusters suspended in liquid metals. The application of such model includes manufacturing of metal-matrix composites (MMC), where understanding of the forces acting on particles is required to prevent the formation of clusters and to disperse the reinforcing particles evenly in the volume of metal melt [1], [2]. Another application is removing the contaminants from liquid metal [3]-[5] which can be achieved by combining electro-magnetic (EM) stirring with EM expulsion owing to the fact that the metal is liquid and electrically conducting while the contaminants are solid and non-conducting.

Both applications share the same difficulty: the interaction of the particles with each other and with the walls of the crucible is essential for the outcome of the process, and therefore must be resolved accurately. The elastic forces, friction and cohesion between the particles dictate whether the clusters of particles form or break in the case of MMCs, while in the second case the efficiency of decontamination largely depends on the ability of the particles to adhere to the walls. The EM stirring is typically quite slow (5-10 cm/s, [5], [6]). In order to trace the particles during the stirring, at least one full cycle of stirring should be simulated, which is of the order of 1s for a 10 cm crucible. The large disparity in time-scales associated with particle collisions on one side, and on fluid flow on the other side, calls for multi-scale analysis of the problem, similar to that proposed in [7].

1.1 Fluid time-scale

In this paper the fluid flow is a consequence of applying the EM fields to electrically conducting liquid metal. EM fields induce electrical current in liquid metal that gives rise to a Lorentz force, which drives the stirring motion. It is assumed, that fluid flow is too slow to affect the imposed EM fields, therefore the EM fields are solved in the amplitude and frequency domain and no time-scale is associated with the EM fields. The fluid flow is modelled by solving the Navier-Stokes equation with an additional term representing the Lorentz force. The fluid time-scale for a 10 cm crucible is then of the order of 1 s. In the time reference of individual particle collisions the flow field can be assumed steady.

1.2 Fluid particle time-scale

If no collisions are happening, the particle motion depends on the fluid-particle interaction forces, where the most prominent contribution is that of the drag force, while other forces include lift and added mass, Magnus effect, pressure gradient force etc. These and other forces are reviewed in e.g. [8]-[13]. Some works involve resolving the fluid particle interaction using fluid mesh elements surrounding the particle [14] [15]. This method is convenient to accurately simulate the local fluid flow around the particle and derive the global fluid particle forces. It is however practical only if particles are larger than fluid flow mesh cells, or in other words, if particle size is comparable to the features of the flow. In this paper, particle's size ranges from 1 nm to 100 μm, while the minimum size of the fluid flow cell is ~3 mm. All the fluid particle interaction forces therefore rely on interpolated values of the fluid velocity and pressure. Under these conditions it is safe to assume that the forces acting on a particle do not significantly change until the particle moves to the distance, comparable to its own size. The fluid-particle time-scale is therefore associated with the particle size and average fluid velocity:

$$T_{fp} = \frac{R_p}{U} \tag{1}$$

To ensure accurate simulation, the fluid-particle time-step then must be

$$\Delta_{fp}t = C_{fp}\frac{R_p}{U} \tag{2}$$

Where $C_{fp}\leq 1$ is a parameter. For particles of 1μm radius immersed in the fluid stirred on average at U=5 cm/s the time-step $\Delta_{fp}t\leq 20$ μs for $C_{fp}=1$. If fluid velocity gradient is large then care should be taken to reflect this in the choice of C_{fp}. Taking $C_{fp}=0.01$ makes $\Delta_{fp}t=200$ ns.

1.3 Collision time-scale

The average collision time can be estimated based on the Young's modulus (E_p), particle radius (R_p), density (ρ_p) and approach velocity (U) [7]

$$T_c = 2R\left(\frac{\rho_p^2}{UE_p^2}\right)^{\frac{1}{5}} \tag{3}$$

For two SiC particles of 1μm radius approaching each other at U=5 cm/s the collision time T_c=2ns. Equation (1) is of course an approximation, as it does not take into account the impact angle, tangential forces, spin of the particles, adhesion force, surrounding fluid and presence of other particles. To ensure the accuracy of force transmission during the collision of particles, the time-step in modelling must be associated with the Rayleigh wave speed V_r [16]:

$$\Delta_c t = C_r\frac{\pi R_p}{2V_r}, \tag{4}$$

Where R_p is the particle radius, and $C_r\leq 1$ is a proportionality coefficient. Approximation of the Rayleigh wave speed V_r using the material Poisson's ratio ν was presented by e.g. [17]:

$$V_r \approx \frac{256}{293} + \nu\left(\frac{60}{307} - \nu\left(\frac{4}{125} + \nu\left(\frac{5}{84} + \frac{4}{237}\nu\right)\right)\right) \tag{5}$$

For SiC particle of 1μm radius and C=1, (2) and (3) give $\Delta_c t$=0.2ns. This is equivalent to $T_c/10$, so C=1, 0.5 and 0.1 corresponds to modelling collision in 10, 50 or 100 time-steps. The ratio between the collision and fluid-particle time-steps is then

$$\frac{\Delta_{fp}t}{\Delta_c t} = 10000 \tag{6}$$

Which totally justifies the multi-scale approach.

2 REVIEW OF ADHESION THEORIES

Bradley [18] first described the van der Waals force acting between two rigid spheres in contact and calculated the pull off force as $P_c=4\pi\gamma R$, where γ is interfacial energy of the contacting materials [1] and R is the radius of the sphere.

Derjaguin [19] pointed out that elastic deformations of the spheres need to be accounted for as well as the adhesive interactions. He presented the first attempt to consider the problem of adhesion between elastic spheres: calculating the deformations of the spheres using Hertzian contact theory, he evaluated the work of adhesion assuming only the pair-wise interactions of the closest surface elements. The interaction energy between small elements of curved surfaces was assumed the same as for parallel planes which is known as the Derjaguin approximation.

On the other hand, Johnson [20] made an attempt to solve the adhesive contact problem by combining the Hertzian spherical contact problem and the problem of a rigid flat-ended punch. Johnson et al. [21] applied Derjaguin's idea to equate the work done by the surface attractions against the work of deformation in the elastic spheres to Johnson's [20] combined stress superposition. This resulted in the creation of the famous **JKR** (Johnson, Kendall, and Roberts) theory of adhesive contact [21]. According to them the attractive adhesion force is acting only over the contact area and significantly affects the shapes of the contacting spherical bodies. The pull

[1] The formulae for the pull off force of adhered particles are often used with the notation $\Delta\gamma$ which is the *work of adhesion*. For spheres of the same material $\Delta\gamma\approx\gamma/2$, therefore $P_c=2\pi\Delta\gamma R$

off force calculated using JKR model is $P_c=3\pi\gamma R$. The contact area is a circle with radius a, defined as follows:

$$a^3 = \frac{3R}{4E}\left[P + 6\pi\gamma R + \sqrt{12P\pi\gamma R + 36\pi^2\gamma^2 R^2}\right], \quad (7)$$

where P is the applied normal load and E is the combined Young's modulus. Hertzian theory evaluates the contact radius simply as $a^3=3PR/4E$, therefore JKR theory is reduced to Hertzian if adhesion is neglected, i.e γ=0.

Derjaguin et al [22] developed a contact theory (**DMT –** Derjaguin, Müller, Toporov) that combined Bradley's adhesion force with Hertz elastic contact theory. The attractive intermolecular force is assumed applicable in the contact area as well as in the surrounding annulus zone. The resulting profile of the deformed spheres remains Hertzian and the pull off force is equal to the one derived by Bradley, $P_c=4\pi\gamma R$. The contact radius is then given by

$$a^3 = \frac{3R}{4E}[P + 4\pi\gamma R] \quad (8)$$

Qualitative analysis of both JKR and DMT models performed by Tabor [23] as well as more detailed analysis based on the Lennard-Jones potential conducted by Muller et al [24] showed that the contradiction between the models lies in the physical principles of adhesive contact assumed by the authors. Both Tabor and Muller concluded that the adhesive contact of larger, softer bodies with stronger surface interaction can be described by the JKR model, while the DMT model is applicable to the smaller, harder bodies with weaker surface interaction. Parameters τ, μ were introduced in [23] and [24] to determine which model is more appropriate:

$$\tau \cong \left[\frac{R\gamma^2}{E^2 z_0^3}\right]^{1/3}, \ \mu = \frac{32}{3\pi}\left[\frac{2R\gamma^2}{\pi E^2 z_0^3}\right]^{1/3}, \quad (9)$$

where z_0 is the equilibrium separation distance, typically 0.16-0.4 nm [25]. According to Muller if μ<1 then DMT is applicable whereas if μ>>1 it is JKR.

Maugis [26] suggested a smooth transition model between JKR and DMT approaches which exploits the principles of fracture mechanics. For simplicity, Lennard-Jones interaction potential is replaced by the step-function, which is known as Dugdale approximation. Greenwood and Johnson [27] suggested an alternative model to Maugis based on a combination of two Hertzian profiles that also connect both the JKR and DMT models in one general theory. These two models use a parameter, which defines the area where the adhesion force is applicable. The necessity to evaluate this parameter at every time step during particle collision makes it impractical to use either Maugis [26] or Greenwood and Johnson [27] theories in a DEM solver. Therefore in the present paper the JKR and DMT models are implemented and the Müller parameter μ is used to determine which one is more applicable.

3 CONTACT MECHANICS

3.1 Oblique loading without adhesion.

The most commonly used particle contact model was first introduced by Cundall and Strack [28] in attempt to predict the complex behaviour of sand specimens under loading and unloading. They suggested treating sand particles as spheres which can move individually and interact only at the contact spots. The contact model consisted of linear spring elements as well and viscous damping elements in both normal and tangential directions, as shown schematically in Figure 1a. The modifications of this model are reviewed in e.g. [9][10]. The developments of this approach can include addition of rolling and twisting resistance [7] which are neglected in this paper.

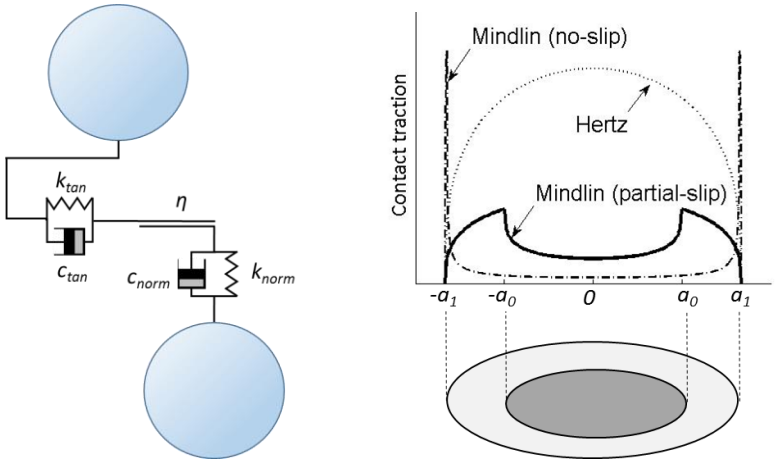

Figure 1 (a) Commonly used spring-dashpot and sliding element model; (b) contact traction distribution of two contacting spherical bodies according to the Mindlin and Deresiewicz model. ▩ - indicates circular zone with radius a_0 where elastic tangential force is applicable, □ - indicates the ring-shaped micro-slip area with external radius a_1..

While being extensively used in CFD-DEM simulation codes such as developed by Goniva, Kloss, Hager, Wierink and colleagues [12], [13], this model has a number of disadvantages. Firstly, accurate description of the contact between spherical bodies given by Hertz predicts non-linear normal elastic stiffness as $k_n=2E^*a$, where E^* is the combined Young's modulus and a is the radius of the (circular) contact area. It is noted in [7] that for small deformations Cundall and Strack model works well, although it is not obvious how to correlate the constant elastic stiffness values k_{norm}, k_{tan} and viscous damping coefficients c_{norm}, c_{tan} with properties of the materials involved. In addition to that, this paper considers nano- and micro-particles of sizes 50 nm to 100 μm, and therefore adhesion force must be incorporated. All of the adhesion models mentioned in the Section 2 of this paper are based on Hertz elastic theory. For these reasons, Hertz theory is used in this paper to evaluate the relationships between normal force and displacement as well as contact area.

The tangential contact forces are implemented in this paper by means of the Mindlin and Deresiewicz theory [29]. It is assumed that two elastic spheres in tangential contact experience a partial-slip, where the total force is a combination of elastic tangential force in the circular area in the centre of the contact zone and sliding friction force in the ring shaped exterior of the contact zone. Once the partial-slip tangential force exceeds the total sliding friction force, the bodies slide relative to each other. The tangential force in this case is then equivalent to the sliding friction force $F_s=\eta P$, where η is the friction coefficient, P is the normal load. The distribution of contact traction is illustrated in Figure 1b.

Thornton and Yin [30] combined all the major cases of the loading/unloading conditions described by Mindlin & Deresievicz [29] and derived the following expression for the tangential stiffness during oblique loading:

$$k^t = 8G^* a\theta \pm \eta(1-\theta)\frac{\Delta P}{\Delta \delta_t} \tag{10}$$

where G^* is the combined shear modulus, a is the contact radius, η is the friction coefficient, ΔP is the increment of the normal load, $\Delta\delta_t$ is the increment of the tangential displacement and θ is a parameter defining the ratio of the elastic force to the micro slip friction force. The parameter θ depends on the loading history and is defined as follows:

$$\theta^3 = 1 - \frac{T + \eta\Delta P}{\eta P}; \qquad \theta^3 = 1 - \frac{T^* - T + 2\eta\Delta P}{2\eta P}; \qquad \theta^3 = 1 - \frac{T - T^{**} + 2\eta\Delta P}{2\eta P}, \tag{11}$$

for loading for unloading for reloading

where T is current value of the tangential force and T^* and T^{**} are the load reversal points. Normal elastic stiffness is defined as $k^n=2E^*a$ according to Hertz theory; see [30] for details.

3.2 Oblique contact with JKR adhesion

Savkoor and Briggs [31] extended the JKR contact theory to consider the effect of adhesion in the case of oblique loading. It was suggested that applying the tangential force reduces the potential energy by an amount of $T\delta_t/2$. Adding this term to the JKR energy balance equation modified the contact radius (7) as:

$$a^3 = \frac{3R}{4E}\left[P + 6\pi\gamma R \pm \sqrt{12P\pi\gamma R + 36\pi^2\gamma^2R^2 - \frac{T^2E}{4G}}\right] \tag{12}$$

It was concluded that in the presence of tangential force, the contacting spheres peel off each other thus reducing the contact area. The peeling process continues until T reaches the critical value of

$$T_c = 4\sqrt{(3P\pi\gamma R + 9\pi^2\gamma^2R^2)\mathrm{G/E}}. \tag{13}$$

For the normal load Thornton and Yin [21] have adopted the JKT theory. The stiffness is then evaluated as

$$k^n = 2E^*a\left[3 - 3\left(\frac{a_c}{a}\right)^{\frac{3}{2}}\right] / \left[3 - \left(\frac{a_c}{a}\right)^{\frac{3}{2}}\right] \tag{14}$$

where $a_c=9\pi\gamma R^2/4E$ is the JKR contact radius at the moment of separation (pull off radius).

In the case of oblique loading Thornton and Yin [30] followed [31] in what concerns the peeling process. They however assumed that once the peeling process is complete, the contacting bodies operate in the partial slip regime as described before with the difference that the normal force P is replaced with $P+6\pi\gamma R$.

3.3 Oblique contact with DMT adhesion.

In this paper it is suggested to combine the Thornton and Yin [30] partial slip no adhesion model with DMT adhesion. The DMT theory assumes that the deformed shapes of the contacting bodies remain within Hertzian elastic theory. Therefore a no-adhesion model [30] was adopted where the normal force P is replaced with $P+4\pi\gamma R$ to account for the adhesion force. This approach considers instantaneous separation of the particles, as opposed to the JKR theory, where particles stretch elastically prior to pulling off. The maximum stretching in the JKR case is evaluated as $\delta_c = \left(\frac{3\pi^2\gamma^2R}{16E^2}\right)^{1/3}$ whereas $\delta_c=0$ in the DMT case. The effect of the stretching prior to separation is illustrated in [2].

4 VISCOUS DRAG

The momentum of the fluid is transferred on the particles via the drag force. Di Felice's [32] theory is used to account for the effect of presence of other particles. Drag force on a single

particle in a flow with relative velocity $v = v_f - v_p$, where v_f, v_p are the velocities of the fluid and the particle, can be evaluated as follows:

$$\begin{aligned} F_d &= \frac{1}{2}\rho_f v^2 \mathrm{C}_d \pi R_p^2 \varepsilon^{-\beta} \\ \mathrm{C_d} &= \left(0.63 + \frac{4.8}{\sqrt{\mathrm{Re_p}}}\right)^2 \\ Re_p &= \frac{\rho_f}{\mu_f}\alpha_f R_p |v_f - v_p| \end{aligned} \tag{15}$$

where Re_p is the particle Reynolds number, μ_f and ρ_f are dynamic viscosity and density of the fluid, ε is the void fraction value, C_d is the drag coefficient for spherical particles, and function $g(\varepsilon) = \varepsilon^{-\beta}$ is a measure of how much the drag force is affected by the presence of other particles. Empirical parameter β was evaluated to fit the experimental data for a wide range of Reynolds numbers (10^{-2} to 10^4) and void fraction values (0.4 to 1):

$$\beta = 3.7 - 0.65e^{-0.5\left(1.5 - log_{10} Re_p\right)^2} \tag{16}$$

In the literature, modifications of $g(\varepsilon)$ are used, such as $g(\varepsilon) = \varepsilon^{1-\beta}$ [10], $g(\varepsilon) = \varepsilon^{2-\beta}$, [12], [13], or $g(\varepsilon) = \varepsilon^{-1-\beta}$ [11]. Di Felice noted however that in the case of the flow through random packed spheres ($\varepsilon \approx 0.4$), Ergun's equation predicts $g(0.4) = \frac{14.6}{C_d}\left(1 + \frac{51.4}{Re_p}\right)$. For a wide range of Reynolds numbers $g(0.4)$ is best predicted by $g(\varepsilon) = \varepsilon^{-\beta}$. In e.g. Stokes drag formula is used multiplied by $g(\varepsilon) = \varepsilon^{-\beta}$ [7]. If the void fraction ε is close to unity, which is true for dilute suspensions, the choice of $g(\varepsilon)$ does not significantly affect the resulting drag force value.

The void fraction value ε is typically evaluated based on the density of particles in a mesh cell (see e.g. [12], [13]). In the present model the CFD mesh is not defined, therefore the void fraction is evaluated based on the particles located within $10R_p$ distance of the current particle centre.

5 PREDICTING PARTICLE COLLISIONS

5.1 Computational model

In order to obtain the positions, orientations, linear and angular velocities of the particles, the linear and angular momentum equations are solved:

$$\begin{aligned} m_p \frac{dv}{dt} &= F_0 + F_{fp} + F_c \\ I_p \frac{d\omega}{dt} &= M_{fp} + M_c \end{aligned} \tag{17}$$

where m_p and I_p are particle mass and moment of inertia, v and ω are linear and angular velocities, F_{fp} and M_{fp} and F_c and M_c are total force and torque acting on the particle due to fluid particle interaction and collisions respectively, while F_0 is a sum of other forces, such as gravity or buoyancy. Equations (17) are discretized up to second order terms for positions and orientations and first order terms for velocities:

$$\begin{aligned} P(t_0 + \Delta t) &= P(t_0) + v(t_0)\Delta t + \frac{1}{2}\Delta_{fp} t^2 \frac{F(t_0, v_0)}{m_p} \\ v(\mathrm{t_0} + \Delta t) &= v(t_0) + \Delta t \frac{F(t_0, v_0)}{m_p} \end{aligned} \tag{18}$$

where P is particle position vector, $F = F_0 + F_c + F_{fp}$ is total sum of forces, t_0 – current time and Δt time-step. It is not defined at this stage whether Δt is a fluid- particle or collision time-step.

For the equations for particle orientation and angular velocity the position must be replaced with orientation, velocity by angular velocity, forces by torques and mass by moment of inertia.

5.2 Multi-scale approach

The multi-scale approach is implemented is a similar way to that in [7]. Authors of [7] consider fluid, particle and collision time-steps, where collision time-step is used only for the particles that collide. The workflow of the method is schematically illustrated in Figure 2. The same method with minor modifications is implemented by the authors of this paper and is presented in Section 5.3. Fluid time-step is not applicable in this paper as the fluid flow is assumed steady. One way coupling is implemented from the fluid scale to fluid-particle scale, i.e. the effect of particle motion on the fluid flow is considered negligible in this paper. The term "particle time-step" in [7] is replaced by the authors with "fluid-particle time step" in this paper as it seems to be less confusing. From the description of the method [7] it follows that the collision time-step is applied to the particles as soon as they are identified as colliding, i.e. at the beginning of the fluid-particle time-step. In the case where the ratio between collision and fluid-particle time-steps is $\Delta_{fp}t/\Delta_c t \approx 10000$, modelling the motion of the particle using the collision time-step before the actual collision is an unnecessary waste of CPU time.

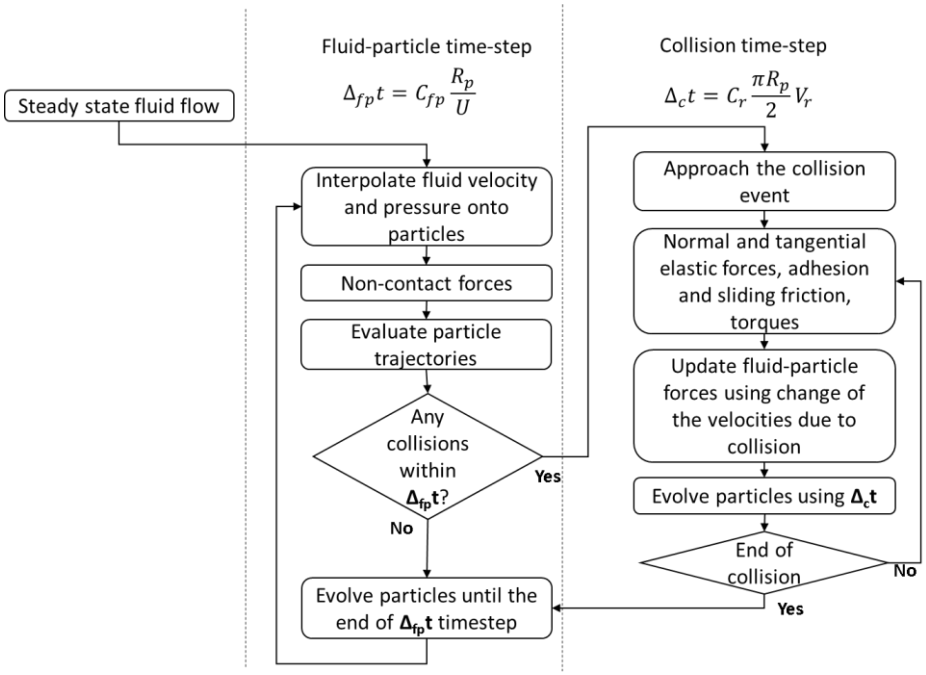

Figure 2 Work-flow of an algorithm with fluid-particle and particle collision timesteps

Section 5.4 presents a method where not only the collision pairs (particle-particle or particle-wall) are identified, but also the time of collision is evaluated. This allows to advance the colliding particles to the moment of their collision using the non-contact forces evaluated at the fluid-particle time-step. Then, the collision is resolved using collision time-step and particles are advanced to the end of the fluid-particle time-step. Most of the fluid-particle interaction forces are based on the relative velocity and spin of particle and fluid. In both methods therefore care should be taken to recalculate these forces using the velocity, direction of motion and spin modified due to collision. Both methods presented in Sections 5.3 and 5.4 are called "dilute" because they operate under the assumption that a colliding pair does not affect any other particles. This assumption holds provided that collisions are well dispersed in space and/or time.

This brings us to the method described in Section 5.5. It combines the benefits of time-step and event-driven methods. Event-driven methods are used in modelling granular gases or molecular dynamics [33], where collisions are rare and collision time is small in comparison to the global time-scale of the problem. The method considers identifying the whole sequence of collisions. Starting from the earliest collision, all the particles are advanced to the time of collision. After collision is resolved using the collision time-step, the trajectories of the colliding and neighbouring particles are re-evaluated. New collisions might be added to or removed from the sequence due to the changes in trajectories. The procedure is then repeated for the next collision in the sequence. The work-flow of the method is illustrated in Figure 3 .

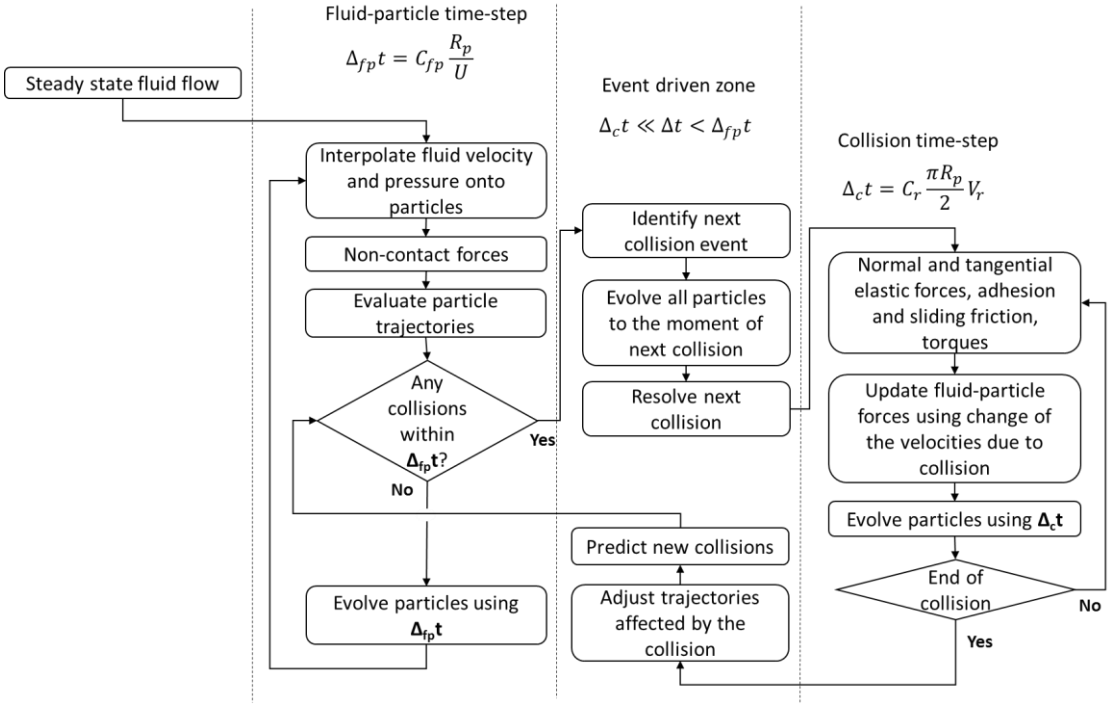

Figure 3 A combined time-step and collision event driven method: fluid particle forces evaluated every fluid-particle time-step are used for predicting particle trajectories; collisions are resolved using collision time-step; when particles are not colliding, the system of particles evolves from one collision event to another until the end of the fluid-particle time-step..

5.3 Linear dilute method

Let particles positions at the time t_0 at the beginning of the fluid-particle time-step be $P_1(t_0)$ and $P_2(t_0)$. Equation (18) then renders

$$P_i(t_0 + \Delta_{fp}t) = P_i(t_0) + v_i(t_0)\Delta_{fp}t + \frac{1}{2}\Delta_{fp}t^2\frac{F_i(t_0)}{m_i}, i = 1,2 \quad (19)$$

The trajectories of the particles within the fluid-particle time-step $\Delta_{fp}t$ are then parabolic curves connecting $P_i(t_0)$ with $P_i(t_0+\Delta_{fp}t)$. For simplicity, let us assume, that particles move along the straight lines connecting $P_i(t_0)$ with $P_i(t_0+\Delta_{fp}t)$ as shown in Figure 4a.

These straight lines can be parameterized for $t \in [t_0, t_0 + \Delta_{fp}t]$ as:

$$P_i(t) = P_i(t_0) + v_i^* t \quad (20)$$

where v_i* is given by:

$$v_i^* = \frac{P_i(t_0+\Delta_{fp}t)-P_i(t_0)}{\Delta_{fp}t} = v_i(t_0) + \frac{1}{2}\Delta_{fp}t\frac{F_i(t_0)}{m_i} \quad (21)$$

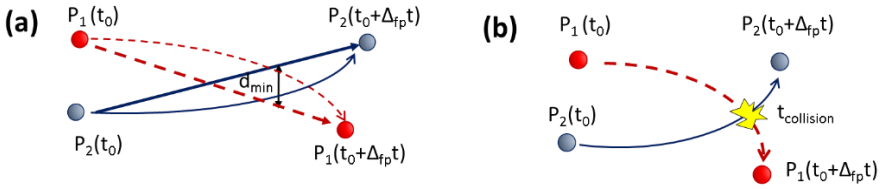

Figure 4 (a) Predicting particle collisions using the closest distance between (a) straight line approximation of particle trajectories; (b) parabolic trajectories of the particles

Note, that this linear approximation of the trajectory is different to that, obtained using first order terms for particle positions, as $v_i^*(t_0)=(v_i(t_0)+ v_i(t_0+\Delta_{fp}t))/2$. Assuming that particles are moving along a parameterized line defined by equation (20), the distance between them can be evaluated as [34]:

$$d(t) = |P_1(t) - P_2(t)| = \left|P_1(t_0) - P_2(t_0) + t\left(v_1^*(t_0) - v_2^*(t_0)\right)\right| \tag{22}$$

The "closest point of approach" as it is described in [34] is reached when $d(t)$ is minimum, therefore $d(t)^2$ is minimum:

$$d(t)^2 = t^2\left(v_1^*(t_0) - v_2^*(t_0)\right)^2 + 2t\left(P_1(t_0) - P_2(t_0)\right)\cdot\left(v_1^*(t_0) - v_2^*(t_0)\right) + \left(P_1(t_0) - P_2(t_0)\right)^2 \tag{23}$$

where "$\cdot$" denotes the dot product, and power of two denotes dot product of a vector with itself. Since $d(t)^2$ is minimum, the derivative must be equal to zero:

$$0 = 2\frac{d}{dt}dt = 2t\left(v_1^*(t_0) - v_2^*(t_0)\right)^2 + 2\left(P_1(t_0) - P_2(t_0)\right)\cdot\left(v_1^*(t_0) - v_2^*(t_0)\right) \tag{24}$$

which gives a solution $t=t_{cpa}$

$$t_{cpa} = -\frac{2\left(P_1(t_0)-P_2(t_0)\right)\cdot\left(v_1^*(t_0)-v_2^*(t_0)\right)}{\left|v_1^*(t_0)-v_2^*(t_0)\right|^2} \tag{25}$$

The minimum distance $d(t_{cpa})$ is then compared to the sum of the particle radii R_1+R_2. If $d(t_{cpa})>R_1+R_2$ then there is no collision. If $d(t_{cpa})\leqslant R_1+R_2$ and t_{cpa} is within the fluid-particle time-step then the collision occurs. If $d(t_{cpa})\leqslant R_1+R_2$ and t_{cpa} is out of the range of the fluid-particle time-step, then various scenarios are possible, which are illustrated schematically in Figure 5. Equation (22) defines a parabola facing upwards. If therefore, $t_{cpa}<t_0$ then $d(t)$ is increasing monotonously within the fluid-particle time-step, and it is only necessary to check whether collision occurs at the beginning of the fluid-particle time-step. If however $t_{cpa}>t_0+\Delta_{fp}t$ then $d(t_0+\Delta_{fp}t)$ should be tested for collision.

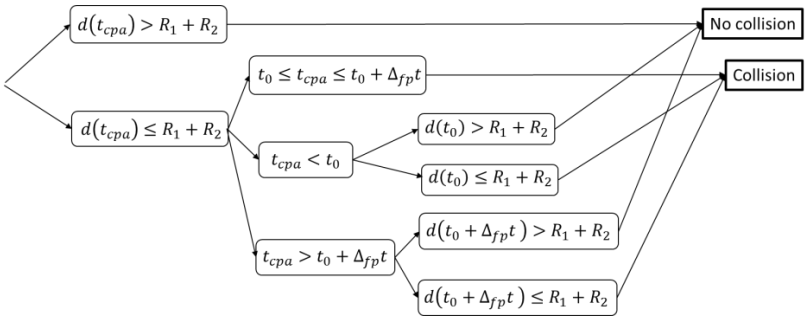

Figure 5 Set of conditions that the closest approach distance between particles is tested against

This method is the easiest for implementation among those considered in this paper. However, as a consequence of approximating the trajectories of the particles by the straight lines, the collision predictions are not accurate. Particles moving along the parabolic trajectories may

collide a time different to the predicted one, or not collide at all. The collision event is approached in a series of collision time-steps. The particles tagged as colliding are then advanced using the collision time-step until they have collided or until the end of the fluid-particle time-step is reached. The particle collisions are identified only at the beginning of the fluid-particle time-step. If collision of the particles changes their trajectories in a way that creates new non-predicted collisions, or renders some of the predicted collisions obsolete, this will not be reflected in the analysis. Reasonable accuracy can then be achieved with the optimal fluid-time particle step chosen by the cost of computation. The method has also been found efficient for a dilute concentration of particles, where collisions of more than two bodies (three particles or two particles and a wall) are negligibly rare.

5.4 Quartic dilute method

This method is similar to the linear dilute method described in Section 5.3 and the workflow is the same as represented diagrammatically in Figure 2. The only differences are how the collisions are identified and how the collision events are approached. In this method the trajectories as given by Equation (19) are not approximated by straight lines as shown in Figure 4a but treated as parabolic (Figure 4b). The squared distance between the particles is compared to the squared sum of the radii:

$$|P_1(t) - P_2(t)|^2 = (\mathrm{R}_1 + R_2)^2 \tag{26}$$

Equation (26) is a quartic equation in t:

$$\mathrm{A}_4 t^4 + A_3 t^3 + A_2 t^2 + A_1 t + A_0 = 0 \tag{27}$$

where

$$A_4 = \frac{1}{4}\left(\frac{F_1}{m_1} - \frac{F_2}{m_2}\right) \cdot \left(\frac{F_1}{m_1} - \frac{F_2}{m_2}\right)$$

$$A_3 = (v_1 - v_2) \cdot \left(\frac{F_1}{m_1} - \frac{F_2}{m_2}\right)$$

$$A_2 = (v_1 - v_2) \cdot (v_1 - v_2) + \big(P_1(t_0) - P_2(t_0)\big) \cdot \left(\frac{F_1}{m_1} - \frac{F_2}{m_2}\right)$$

$$A_1 = 2\big(P_1(t_0) - P_2(t_0)\big) \cdot (v_1 - v_2)$$

$$A_0 = \big(P_1(t_0) - P_2(t_0)\big) \cdot \big(P_1(t_0) - P_2(t_0)\big) - (R_1 + R_2)^2$$

Note that particle positions P_1 and P_2, velocities v_1 and v_2, and forces F_1 and F_2 are vectors, and "$\cdot$" denotes dot product.

Equation (27) is then solved analytically for real roots using the algorithm adapted for computations [35]. The method developed in [35] is easy to implement and far less computationally expensive than the classic Cardano-Ferrari formulae for quartic equations. Equation (27) has none, or one to four real roots. If there are no real roots, the trajectories of the particles do not intersect. The smallest real root fitting into the range of the fluid-particle time-step $t \in [t_0, t_0 + \Delta_{fp} t]$ is used as a collision time for a pair of particles. Note that conditions shown in Figure 5 do not have to be checked, as the solution of (27), if exists, represent the moment of collision, rather than the shortest approach distance between trajectories as in Section 5.3

For particle collisions with walls that are represented by planes, Equation (27) is reduced to quadratic equation. If walls and other geometrical features of the problem are represented by (parts of) spheres, cylinders or cones, then a quartic equation different to (27) must be solved, which is not covered in this paper.

This method saves computational time because the colliding particles are advanced to the moment of collision in one step rather than in a long series of collision time-steps. This method however shares the same disadvantage with the linear dilute method: particle collisions are predicted at the beginning of the fluid particle time-step and the predictions are not corrected due to collisions that have occurred previously.

5.5 Quartic collision driven method

This method is a development of the quartic dilute method (Sections 5.4) which takes into account the effect of the particle collision on other predicted collisions. For this purpose the collision that occurs first is identified. All the particles are then advanced to the moment of collision and the collision is resolved using the collision time-step. The new trajectories for all the particles are computed and the process is repeated until the end of the fluid-particle time-step. Additional modification allows to re-evaluate only the trajectories of the neighbouring particles.

The work-flow of the method is schematically illustrated in Figure 3. The collision loop stops or interrupts ("end of collision" block in the diagram) if one of three conditions are met: (a) particles have separated, (b) particles have stuck to each other (or to the wall), (c) collision took a certain number of time-steps (parameter) and is not yet resolved. Condition (c) is of particular importance if particles oscillate during the collision until the balance between attractive-adhesive and repulsive-elastic forces is achieved. If oscillation takes a long time, the collision loop must be interrupted in order to re-evaluate the fluid-particle forces and update the collision predictions. Condition (b) is met if a decaying oscillation between particles (or a particle and a wall) is detected. This condition is essential in the case where particles stick to the walls and remain there: particles that are stuck can then be removed from the computation cycle.

6 SIMULATION RESULTS

Earlier work by authors [2] considered the effect of the shock waves on dense agglomerates of particles in the context of de-agglomeration of ceramic nano-reinforcements in the production of aluminium based metal-matrix nano-composites [1]. The effect of the choice of adhesion model (JKR or DMT) was studied for a two-dimensional case of 36 densely packed particles as well as the effects of size, material properties and characteristics of the shock wave pulse [2]. The developments presented in the current paper are aimed at up-scaling the time and dimensions of the simulated problem. First, a test case is presented where particles are stirred using electro-magnetic fields (Section 6.1). In Section 6.2 the execution time is compared for the collision prediction methods described in Sections 5.2-5.5.

6.1 Electro-Magnetic Stirring of SiC particles

Test case considered in this paper simulates 216 SiC particles suspended in liquid silicon in the context of recycling of PV silicon kerf. The technique that is being developed in the project [3] aims to remove the SiC contaminants with the help of EM stirring. In brief, the solid non-conducting SiC particles approach the crucible walls as they move with the stirring flow of liquid silicon. Particles stick to the walls due to adhesion force and can be easily removed from the solidified silicon ingot by polishing the surface. The EM stirring (both the EM part and the fluid flow) has been modelled using the finite volume method which is described in detail in [36]. The current paper concentrates on the fluid-particle interaction and particle collisions only.

Initially, 216 particles are located in the nodes of a 6×6×6 grid as shown in Figure 6a. The pressure contours and velocity vectors obtained for the case of EM stirring of liquid silicon are shown in Figure 6b. Two distinct stirring poloidal motion patterns are indicated by arrows in

Figure 6b. Figure 7 (a) and (b) present the positions of particles after 10 seconds of stirring: (a) particles radius is 100 μm, (b) 10 μm. Black particles are those stuck to the walls or bottom of the crucible. Two conclusions can be drawn from Figure 7 (a) and (b). First, that larger, i.e. heavier, particles of 100 μm radius (Figure 7 (a)) sink to the bottom of the crucible before they get carried by the stirring motion. Second, that 10 seconds of stirring is clearly not sufficient to push all the particles towards the walls, thus allowing them a chance to stick. In reality, silicon is slowly cooled down, and stirring may last for several hours, giving plenty of time for the particles to stick to the walls. Several hours of processing is however rather large time-scale for modelling. The execution time of the simulation software for 10 second of real time is presented in the next section.

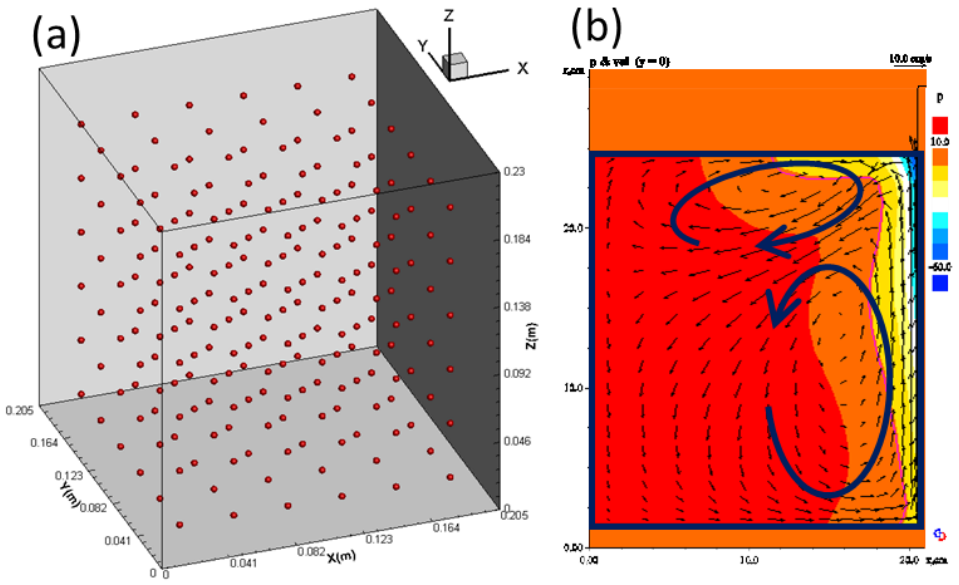

Figure 6 (a) Initial distribution of 216 particle (not to scale) located in the nodes of a 6x6x6 mesh within a cuboid domain of 20.5×20.5×23 cm^3 (b) fluid pressure contours and velocity vectors in a 41×41×23 cm^3 crucible; quarter of the crucible is shown, assuming symmetry conditions with respect to YZ and XZ planes, large arrows schematically indicate the sense of poloidal motion caused by EM stirring.

6.2 Execution time of collision prediction algorithms

In this section the execution time for 10 second of EM stirring of 216 particles suspended in liquid silicon is presented. The developed simulation code has room for significant improvement by utilizing multiple CPUs or a GPU card(s) using message passing interface. Using parallel computing would help to up-scale the model in terms of the number of particles. The algorithms developed in this paper helped to up-scale the model in terms of time and lateral dimensions. The code was tested on a single CPU of a multi-CPU machine based on Intel Xeon, 3.4GHz with 128 GB RAM.

The fluid-particle interaction and collision time-steps are defined as described in Sections 1.2 and 1.3, and therefore proportionally depend on the particle size. It is expected, that provided that all the conditions are similar, including the likelihood and frequency of collisions, the execution time for particles of different sizes should change proportionally with the sizes. This was found to be the case, as shown in the bar chart of Figure 8, where execution times are compared for particles of 100, 10 and 1 μm radii for the three described collision prediction methods, and a direct single-scale method, where no predictions are used and the whole problems is modelled using collision time-step.

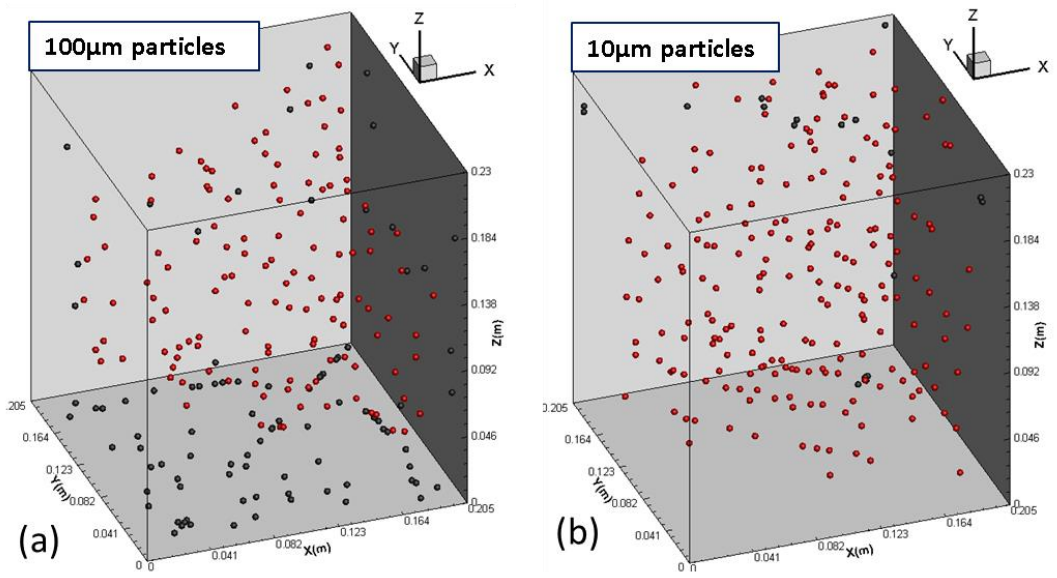

Figure 7 Particles after 10 s of stirring; **black** particles are those stuck to the bottom or walls of the crucible; (a) 100 µm (b) 10 µm; particles are not to scale.

Using the direct method it would take ~ 4 months, ~3.5 years and ~34 years to complete the simulation. The execution was halted after 48h of running and the total execution time was estimated based on the progress made so far. Using collision prediction models the simulation took approximately 45 min, 9 h and 90 h for particles of 100, 10 and 1 µm radii respectively, which is faster than the direct method by a factor of ~3000. Note that time-step coefficients C_{fp} =0.01 (2) and C_r =0.01 (4) were used, i.e. at least 100 time-steps to resolve an average estimated collision event. Increasing the coefficients up to e.g. 0.1 would decrease the simulation time by a factor of 10. There is also room for potential improvement of the code, which includes optimizing loops structure and data storage as well as using parallel computing. Main aim of this test case is to compare the prediction methods.

Owing to a very dilute concentration of particles, there was no noticeable difference in the particle trajectories. In fact, no predictions were compromised by the presence of other particles, i.e. the quartic dilute method gave perfectly accurate result, which might not be the case for a larger number of particles, if the initial positions are more concentrated, or if the fluid flow causes local concentrations of particles. The quartic dilute method was always the fastest due to the fact that particles were advanced to the exact moment of their collision and in spite of the fact that solving quartic equation requires extra algebraic operations and therefore is more computationally expensive. When using the collision driven method, time is lost due to re-evaluating the particles trajectories after each collision, which in general (not dilute) systems is expected to give a more accurate result. Linear dilute is algebraically the easiest, but time is lost when approaching the collision event in collision time-steps. Minor differences in the execution time for the prediction methods were: 45 minutes for linear dilute, 40 min for quartic and 43 min for collision driven methods for 100 µm particles; 10 h, 8 h 30 min and 9 h 20 min respectively for 10 µm particles, and 90 h, 84 h and 91 h for the smallest, 1 µm particles. The execution times are shown in Figure 8. Note that the execution time of a model that uses direct method goes far beyond the chart.

Figure 8 demonstrates that using the direct method results in unreasonably long computational time, while all of the prediction methods take approximately the same time. The quartic collision driven method although somewhat more complex in implementation is an obvious choice as it gives accurate predictions as opposed to the "dilute" methods.

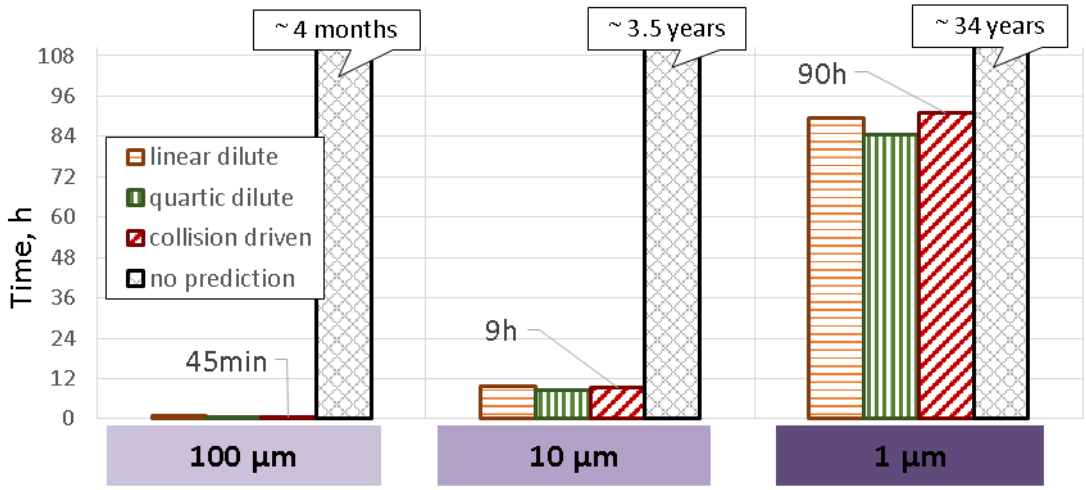

Figure 8 Comparison of the execution times for 10 seconds of real time simulation for linear dilute, quartic dilute, quartic collision driven and direct methods. Bars corresponding to the direct method case go well beyond the chart.

7 CONSLUSIONS

This paper considers CFD-DEM modelling of particles suspended in liquid metals. Dense agglomerates of particles are studied in detail in an earlier paper [2], while the current paper concentrates on the problem where concentration of particles is dilute, but the time and dimensions are large in comparison to the particle size and collision time. Multiple time-scale approach was implemented and three collision prediction methods are developed. Two methods are based on resolving the particle collisions independently, assuming that each collision is not interfering with other particle. These methods are called dilute as they are applicable to the dilute systems of particles only. The third method combined the benefits of time-step and event driven modelling. This method is also applicable to dense systems of particles, although the efficiency has not been tested. The execution time for the three prediction methods was compared and it was found that using multi-scale approach and collision prediction methods reduces the computational time by a factor of ~3000 for dilute systems. The differences in computational time for the three methods were minor, which makes the collision driven quartic method the optimal choice.

ACKNOWLEDGMENTS

The authors acknowledge financial support from the projects ExoMet [1] (co-funded by the European Commission, contract FP7-NMP3-LA-2012-280421 and the European Space Agency) and SIKELOR [3] - funded the European Commission, sub-programme: ENV.2013.6.3–1, project reference 603718.

REFERENCES

[1] http://www.exomet-project.eu/

[2] Manoylov, A., Bojarevics, V., Pericleous, K. A. Modeling the Break-up of Nano-particle Clusters in Aluminium- and Magnesium-Based Metal Matrix Nano-Composites. *Metallurgical and Materials Transactions. A* (2015) 46(7): 2893-2907

[3] http://www.sikelor.eu/

[4] I. Lombardi, F. Tappa, G. Fragiacomo, S. Pizzini, F. Hugo: "Progress in the recycling of silicon fine powders from fixed abrasive operations on Silicon Ingots. *Proc. 26th European PV Solar Energy Conference and Exhibition*, Hamburg, Germany, 2011

[5] Djambazov, G., Pericleous, K., Bojarevics, V., Forzan, M. and Dughiero F, Modeling the Electromagnetic Processing of Recycled Silicon Dust, *TMS Annual Meeting*, Nashville, Tennessee (2016),.

[6] Bojarevics, V., Djambazov, G. S., Pericleous K. A. (2015) Contactless Ultrasound Generation in a Crucible. *Metallurgical and Materials Transactions A*, 46A. pp. 2884–2892. (doi: 10.1007/s11661-015-2824-5)

[7] Marshall, J. S., Discrete-element modelling of particulate aerosol flows. *J. Comp. Physics* (2009) 228:1541-1561

[8] Marshall, J. S. and Li, S. *Adhesive Particle Flow: A Discrete-Element Approach*, Cambridge University Press, New York, 2014

[9] Zhou, Z. Y., Kuang, S. B., Chu, K. W., Yu, A. B. Discrete particle simulation of particle–fluid flow: model formulations and their applicability. *J. Fluid Mech.* (2010) 661: 482–510.

[10] Zhu, H.P., Zhou, Z.Y., Yang, R.Y., Yu, A.B. Discrete particle simulation of particulate systems: Theoretical developments. *Chemical Engineering Science* (2007) 62:3378 – 3396

[11] Kafui, K.D., Thornton, C., Adams, M. J. Discrete particle-continuum fluid modelling of gas-solid fluidised beds. *Chem. Eng. Science* (2002) 57:2395-2410

[12] Goniva C., et al., A MULTI-PURPOSE OPEN SOURCE CFD-DEM APPROACH 8th International Conference on CFD in Oil & Gas, Metallurgical and Process Industries, SINTEF/NTNU, Trondheim Norway, 21-23 June 2011

[13] Hager, A et al. Parallel Resolved Open Source CFD-DEM: Method, Validation and Application. *The Journal of Computational Multiphase Flows*, (2014) 6(1):13-27.

[14] Hill, R. J., Koch, D. L., Ladd, A. J. C. The first effects of fluid inertia on flows in ordered and random arrays of spheres, *Journal of Fluid Mechanics* 448, (2001) pp. 213-241

[15] Hill, R. J., Koch, D. L., Ladd, A. J. C. Moderate-Reynolds-number flows in ordered and random arrays of spheres, *Journal of Fluid Mechanics* 448, (2001) pp. 243-278

[16] Thornton, C., Yin, K.K., Adams, M. J., Numerical simulation of the impact fracture and fragmentation of agglomerates, *J. Phys. D: Appl. Phys.* 29 (1996) 424-435

[17] Pichugin, A. V. Approximation of the Rayleigh Wave Speed. *Unpublished draft* (2008)

[18] Bradley, R. S. The Cohesive force between Solid Surfaces and the Surface Energy of solids *Phil. Mag.* (1932) 13:853–62,

[19] Derjaguin, B. Untersuchungen über die Reibung und Adhäsion, IV. 1. Theorie des Anhaftens kleiner Teilchen. *Kolloid-Zeitschrift* (1934) 69:155-164.

[20] Johnson, K. L. A note on the adhesion of elastic solids. *British Journal of Applied Physics* (1958) 9:199-200.

[21] Johnson, K.L., Kendall, K. and Roberts, A.D. Surface Energy and the Contact of Elastic Solids. *Proceedings of the Royal Society A.* (1971)324:301–13

[22] Derjaguin, B.V., Muller, V.M. and Toporov, Y.P. Effect of Contact Deformations on the Adhesion of Particles. *Journal Colloid and Interface Science* (1975):53(2)

[23] Tabor, D. Surface Forces and Surface Interactions. *Journal Colloid and Interface Science* (1977) 58(1)

[24] Muller, V.M., Yushenko V. S. and Derjaguin, B.V. On the Influence of Molecular Forces on the Deformation of an Elastic Sphere and Its Sticking to a Rigid Plane. *Journal Colloid and Interface Science*. (1980) 77(1)

[25] Israelachvili, J. N., *Intermolecular and Surface Forces*, Academic Press, New York, (1985).

[26] Maugis, D. Adhesion of Spheres: The JKR-DMT Transition Using a Dugdale Model. *Journal Colloid and Interface Science.* (1992) 150(1)

[27] Greenwood, J. A., Johnson, K. L. An alternative to the Maugis model of adhesion between elastic spheres. *J. Phys. D: Appl. Phys*. (1998) 31:3279–3290

[28] Cundall, P. A., Strack, O. D. L. A discrete numerical model for granular assemblies. *Geotechique* (1979) 20(1): 47-65.

[29] Mindlin R. D. and Deresiewicz H. Elastic Spheres in Contact Under Varying Oblique forces. *J. Appl. Mech., Trans. ASME* (1953) 20:327.

[30] Thornton, C., Yin, K. K. Impact of elastic spheres with and without adhesion. *Powder Technology* (1991) 65:153-166

[31] Savkoor A.R. and Briggs, G. A. D. The Effect of Tangential Force on the Contact of Elastic Solids in Adhesion. *Proc. Roy. Soc. A* (1977) 356:103

[32] Di Felice, R. The voidage function for fluid-particle interaction systems. *Int. J. Multiphase Flow*(1994) 20(I):153-159

[33] Poeschel, T., Schwager, T., *Computational Granular Dynamics. Models and Algorithms*, , Springer, Berlin Hiedelberg New York, Ch. 3, p. 135 (2005)

[34] Schneider, P. J., Eberly, D. H., *Geometric Tools for Computer Graphics*, Morgan Kaufmann Publishers, San Francisco, (2003)

[35] H. E. Salzer, "A Note on the Solution of Quartic Equations", *Trans. AMS* (1959)

[36] Djambazov, G., Bojarevics, V., Pericleous K. A. and Croft, N. Finite volume solutions for electromagnetic induction processing. *Applied Mathematical Modelling* (2015),doi: 10.1016/j.apm.2015.03.059